

Patch-recovery filters for curvature in discontinuous Galerkin-based level-set methods

F. Kummer^{*1,2,+} and T. Warburton²

¹ Department of Mechanical Engineering, Technische Universität Darmstadt, Otto-Berndt-Straße 2, 64287 Darmstadt, Germany

² Department of Computational and Applied Mathematics, Rice University, Houston, TX 77005-1892, U.S.A.

⁺ (corresponding author, kummer@fdy.tu-darmstadt.de)

October 13, 2018

Abstract

In two-phase flow simulations, a difficult issue is usually the treatment of surface tension effects. These cause a pressure jump that is proportional to the curvature of the interface separating the two fluids. Since the evaluation of the curvature incorporates second derivatives, it is prone to numerical instabilities. Within this work, the interface is described by a level-set method based on a discontinuous Galerkin discretization. In order to stabilize the evaluation of the curvature, a patch-recovery operation is employed. There are numerous ways in which this filtering operation can be applied in the whole process of curvature computation. Therefore, an extensive numerical study is performed to identify optimal settings for the patch-recovery operations with respect to computational cost and accuracy.

1 Introduction and motivating example

In order to simulate immiscible two-phase flows, one usually has to consider surface tension effects. These induce a pressure jump which is proportional to the total curvature κ of the fluid interface \mathcal{I} . Precisely, the momentum equation for the fluid domains \mathfrak{A} and \mathfrak{B} is given as

$$\frac{\partial}{\partial t}(\rho \mathbf{u}) + \operatorname{div}(\rho \mathbf{u} \otimes \mathbf{u}) + \nabla \psi = \mu \Delta \mathbf{u}, \quad (1)$$

^{*}The autor acknowledges financial support by the German Research Foundation (DFG).

while at the fluid interface $\mathcal{I} = \overline{\mathfrak{A}} \cap \overline{\mathfrak{B}}$ the velocity \mathbf{u} and pressure ψ are coupled via the jump condition

$$\llbracket (\psi \mathbf{I} - \mu (\nabla \mathbf{u} + \nabla \mathbf{u}^T)) \mathbf{n}_{\mathcal{I}} \rrbracket = \sigma \kappa \mathbf{n}_{\mathcal{I}}, \quad (2)$$

see e.g. [10] or [16]. We briefly introduce the notation required for this formula:

- The computational domain $\Omega \subset \mathbb{R}^D$ is decomposed into fluid \mathfrak{A} , fluid \mathfrak{B} and the $(D - 1)$ -dimensional interface \mathcal{I} , i.e. $\Omega = \mathfrak{A} \cup \mathcal{I} \cup \mathfrak{B}$. Regarding this work, we restrict ourselves to the case $D = 2$.
- $\mathbf{n}_{\mathcal{I}}$ denotes the normal vector on \mathcal{I} , oriented so that “it points from \mathfrak{A} to \mathfrak{B} ” and κ denotes the total curvature of \mathcal{I} . We assume \mathcal{I} to be smooth enough, so that both, $\mathbf{n}_{\mathcal{I}}$ and κ are at least in $\mathcal{C}^0(\mathcal{I})$.
- the jump operator for $u \in \mathcal{C}^0(\Omega \setminus \mathcal{I})$ is defined as

$$\llbracket u \rrbracket (\mathbf{x}) = \lim_{\xi \searrow 0} (u(\mathbf{x} + \xi \mathbf{n}_{\mathcal{I}}) - u(\mathbf{x} - \xi \mathbf{n}_{\mathcal{I}})). \quad (3)$$

- μ and ρ denote the dynamic viscosity and the density of the fluid, which are usually constant within either \mathfrak{A} and \mathfrak{B} , but have a jump at the interface.

This setting may be described by a level-set function $\varphi \in \mathcal{C}^2(\Omega)$, which fulfills

$$\begin{cases} \varphi < 0 & \text{in } \mathfrak{A} \\ \varphi > 0 & \text{in } \mathfrak{B} \\ \varphi = 0 & \text{on } \mathcal{I} \end{cases} \quad (4)$$

Then, obviously,

$$\mathbf{n}_{\mathcal{I}} = \frac{\nabla \varphi}{|\nabla \varphi|_2} \quad \text{and} \quad \kappa = \text{div}(\mathbf{n}_{\mathcal{I}}). \quad (5)$$

The latter expression is also called Bonnet’s formula. In dependence of the level-set gradient $\nabla \varphi$ and the level-set Hessian $\partial^2 \varphi$, it can be expressed as

$$\text{div} \left(\frac{\nabla \varphi}{|\nabla \varphi|_2} \right) =: \text{curv}(\nabla \varphi, \partial^2 \varphi) \quad (6)$$

with

$$\text{curv}(\mathbf{g}, \mathbf{H}) = \frac{\text{tr}(\mathbf{H})}{|\mathbf{g}|_2} - \frac{\mathbf{g}^T \mathbf{H} \mathbf{g}}{|\mathbf{g}|_2^3}. \quad (7)$$

Note that by the introduction of φ , the properties $\mathbf{n}_{\mathcal{I}}$ and κ , which were initially only defined on \mathcal{I} , were smoothly extended to the whole domain Ω .

The purpose of this paper is to benchmark various filtering strategies for Bonnet’s formula, based on patch recovery. In order to assess the quality of

a filtering strategy, the L^2 -error in the curvature may only be one property of interest; in addition, we define the following benchmark problem:

$$\left\{ \begin{array}{ll} \Delta\psi = 0 & \text{in } \Omega \setminus \mathcal{I} \\ \llbracket \psi \rrbracket = \sigma\kappa & \text{on } \mathcal{I} \\ \llbracket \nabla\psi \cdot \mathbf{n}_{\mathcal{I}} \rrbracket = 0 & \text{on } \mathcal{I} \\ \psi = 0 & \text{on } \partial\Omega \end{array} \right. \quad (8)$$

This Poisson problem shares some behavior with a two-phase flow problem (1), since it would correspond e.g. to the pressure-projection step of a projection method. It is solved by an extended discontinuous Galerkin method (XDG), details are given in section A.

1.1 Outline for this work

The main motivation for this work is given in section 1.4, where it is demonstrated, for a simple example, that different choices for the level-set-field φ , with equal zero-sets \mathcal{I} , can lead to very different results if just a straightforward projection of the curvature is used. Next, the patch-recovery operation which we employ to overcome this issues is introduced (section 2) and the test setup is defined (section 3.1). Results and a discussion, together with recommendations for the use of patch-recover are given in section 3.2. Finally, in appendix A the discretization of the Poisson problem (8) is given.

1.2 Treatment of surface tension in numerical methods.

In multi-phase flow simulations, surface tension plays an important role as soon as length scales become small enough, e.g. in the range of centimeters and below. Over the previous decade, a huge variety of two-phase flow solvers have been proposed and a significant portion of them uses level-set methods. Some of them use a smeared interface approach – where the piecewise constant properties ρ and μ in eqs. (1,2) are regularized so that their derivatives are finite – like e.g. the works of Herrmann [7]. In contrast to this, extended finite element or discontinuous Galerkin methods use an approximation space that is conformal with the location of the discontinuities, like e.g. done by Gross and Reusken [4]. Common to all this methods is that surface tension forces have to be computed from a level-set field φ .

From a flow-solver perspective, what finally matters is the force which is induced into the momentum balance (1) by surface tension effects. This force is only active at the interface \mathcal{I} itself, i.e. in some finite volume (FV), finite element (FE) or discontinuous Galerkin (DG) discretizations, it usually appears at the right-hand-side of the momentum equation as

$$\oint_{\mathcal{I}} \sigma\kappa\mathbf{n}_{\mathcal{I}} \cdot \mathbf{v} \, dS \quad \text{or} \quad \int_{\Omega} \sigma\kappa\mathbf{n}_{\mathcal{I}} \cdot \mathbf{v}\delta_{\mathcal{I}} \, dV.$$

Here, \mathbf{v} denotes a test function (in 2D FV-methods usually, $\mathbf{v} = (1, 0)$ and $\mathbf{v} = (0, 1)$) while $\delta_{\mathcal{I}}$ denotes a delta-distribution on \mathcal{I} . It is either singular, thereby

both integrals given above are equivalent, or regularized, i.e. ‘smeared out’ in a small neighborhood around \mathcal{J} . Whether a ‘sharp’ or a ‘smeared’ approach is used usually depends on the design of the flow solver, i.e. whether the flow solver represents the density and viscosity jump in a ‘sharp’ or smeared fashion.

However, the evaluation of curvature is not the only way to compute surface tension forces. Using a variant of Stoke’s integral theorem, one can re-express surface tension forces in some control volume $K \subset \Omega$ as

$$\oint_{\mathcal{J} \cap K} \sigma \kappa \mathbf{n}_{\mathcal{J}} \cdot \mathbf{v} \, dS = \oint_{\mathcal{J} \cap K} \sigma (I - \mathbf{n}_{\mathcal{J}} \otimes \mathbf{n}_{\mathcal{J}}) : \nabla \mathbf{v} \, dS - \int_{\partial(\mathcal{J} \cap K)} \sigma \mathbf{s} \cdot \mathbf{v} \, dl, \quad (9)$$

where \mathbf{s} is tangential to \mathcal{J} and normal onto $\partial(\mathcal{J} \cap K)$. and $\int \dots dl$ denotes an integral over the boundary of the surface $\mathcal{J} \cap K$; i.e. in 2D, $\int \dots dl$ it is a 0-dimensional point integral (counting measure) over the two end-points of the line $\mathcal{J} \cap K$, while in 3D it is the 1-dimensional line integral over the boundary of the surface $\mathcal{J} \cap K$. Since $\kappa \mathbf{n}_{\mathcal{J}}$ can also be expressed by the Laplace-Beltrami - operator on the manifold \mathcal{J} – for details, we refer to Gross and Reusken [4] – the reformulation of the surface tension is often referred to as the Laplace-Beltrami approximation of the surface tension terms. The main benefit of this re-formulation is that the right-hand-side of eq. (9) does not depend on second derivatives of φ . This seems very attractive e.g. in a FV-discretization, where the test function is constant and therefore the first term on the right-hand-side of (9) vanishes and the problem is reduced to the computation of tangents \mathbf{s} to \mathcal{J} .

The Laplace-Beltrami formulation also shows good results in the extended finite element (XFEM) context, as demonstrated e.g. by Gross and Reusken [4], Cheng and Fries [2], Sauerland and Fries [12].

However, if the numerical integration over the surface \mathcal{J} becomes more precise – as is the case in this work – equation (9) is also fulfilled numerically and therefore one cannot expect significant ‘filtering properties’ from the Laplace-Beltrami formulation, i.e. any oscillations present in the level-set would be captured equally by both, the left- and the right-hand-side of equation (9).

In the work of Chen et al. [1], a projection of the curvature on the broken piecewise polynomial space is obtained from the relation

$$\int_K \underbrace{\operatorname{div} \left(\frac{\nabla \varphi}{|\nabla \varphi|_2} \right)}_{=\kappa} v \, dV = \oint_{\partial K} \frac{\nabla \varphi}{|\nabla \varphi|_2} \cdot \mathbf{n}_K v \, dS - \int_K \frac{\nabla \varphi}{|\nabla \varphi|_2} \cdot \nabla v \, dV \quad (10)$$

for a test function v and a control volume K with outer normal \mathbf{n}_K . Since this is equivalent to the piecewise polynomial reconstruction of Bonnet’s formula (5), one can expect that it is prone to the same issues as we outline in section 1.4. However, the right-hand-side of equation 10 provides the option to use a non-local flux-formulation for $\frac{\nabla \varphi}{|\nabla \varphi|_2}$ at the boundary integral. This was exploited e.g. by Heimann [5], where an additional diffusion term is incorporated into the non-local projection to deal with discontinuities.

A completely different approach to curvature evaluation is proposed by Heimann et al. [6]. They use an extended DG space – they refer to it as ‘unfitted DG’ – for velocity and pressure, a conventional DG field for the level-set while for curvature computation, they employ finite difference scheme.

The patch-recovery post-processing was first introduced for finite element methods by Zienkiewicz and Zhu [17]. To our knowledge, the only application of patch recovery (see section 2) to curvature evaluation has been demonstrated by Herrmann and Jibben [8]. There, a nodal projection is used, while this work employs an L^2 -projection, making the algorithm independent of any choice of nodes and more general with respect to the shape of the patches. The main achievement of this work is that we also investigate the application of patch-recovery for ‘intermediate’ values, like gradients $\nabla\varphi$ and Hessians $\partial^2\varphi$ of the level-set function φ .

1.3 Piecewise polynomial approximation

For sake of completeness, we briefly introduce the numerical grid as well as the approximation spaces used e.g. for φ or ψ . These are fairly standard, and can be found in similar form in many textbooks, see e.g. Hesthaven and Warburton [9] or Di Pietro and Ern [3]. We define:

- the numerical grid: $\mathfrak{K}_h = \{K_1, \dots, K_J\}$, with h being the maximum diameter of all cells K_j . The cells cover the whole domain ($\bar{\Omega} = \bigcup_j \bar{K}_j$), but do not overlap ($\int_{K_j \cap K_l} 1 \, d\mathbf{x} = 0$ for $l \neq j$). We restrict ourselves to non-curved grids, i.e., each cell K_j can be described as the image of a reference cell K_{ref} under an affine-linear mapping $T_j : \mathbb{R}^2 \rightarrow \mathbb{R}^2$, i.e. $T_j(K_{\text{ref}}) = K_j$;
- the broken piecewise polynomial approximation space of maximum total degree p :

$$\mathbb{P}_p(\mathfrak{K}_h) := \left\{ f \in L^2(\Omega); \forall K \in \mathfrak{K}_h : f|_K = \sum_{0 \leq i+j \leq p} x^i y^j b_{ij}, b_{ij} \in \mathbb{R} \right\} \quad (11)$$

- the broken piecewise polynomial approximation space of maximum degree p :

$$\mathbb{Q}_p(\mathfrak{K}_h) := \left\{ f \in L^2(\Omega); \forall K \in \mathfrak{K}_h : f|_K = \sum_{0 \leq i,j \leq p} x^i y^j b_{ij}, b_{ij} \in \mathbb{R} \right\} \quad (12)$$

- the continuous piecewise polynomial space of order p :

$$\mathbb{Q}_p^{\mathcal{C}^0}(\mathfrak{K}_h) := \mathbb{Q}_p(\mathfrak{K}_h) \cap \mathcal{C}^0(\Omega) \quad (13)$$

- the extended broken approximation space of order p , which is used to discretize the Poisson problem (8):

$$\mathbb{P}_p^X(\varphi, \mathfrak{K}_h) := \mathbb{P}_p(\mathfrak{K}_h)\mathbf{1}_{\mathfrak{A}} \oplus \mathbb{P}_p(\mathfrak{K}_h)\mathbf{1}_{\mathfrak{B}}, \quad (14)$$

where $\mathbf{1}_X$ denotes the characteristic function for set $X \subset \Omega$.

- the projector onto some subspace X of $L^2(\Omega)$ in the L^2 -norm:

$$L^2(\Omega) \ni f \mapsto \text{Proj}_X(f) \in X. \quad (15)$$

- that all derivative operators ($\text{div}(-)$, ∇ , Δ and the Hessian ∂^2) in this work should be understood in a broken sense. We assert that all properties defined here are almost everywhere sufficiently smooth, so that the respective derivatives exist in a classical sense everywhere up to a set of measure zero. Therefore, we do not make the usual distinctions, e.g. between the gradient ∇ and the broken gradient ∇_h .

1.4 Motivating example.

The main issue with using Bonnet's formula is that the results are extremely sensitive to minor disturbances in the level-set function φ , which we are going to illustrate by the following example. The exact interface \mathfrak{I}_{ex} is chosen to be a circle with radius $R = 0.8$ around the origin. Obviously, there are infinitely many choices for φ .

For a sharp-interface method, like the one described in appendix A, the interface \mathfrak{I} has to be a closed surface, therefore it is required that also the numerical representation of the level-set field is at least continuous, i.e. $\varphi \in C^0(\Omega)$. To ensure this, the exact level-set function φ_{ex} is projected onto the continuous piecewise polynomial space $\mathbb{Q}_2^{C^0}(\mathfrak{K}_h)$.

Two representations of a circular interface around the origin with radius $8/10$ are compared, namely:

$$\begin{aligned} \text{case (a): } \varphi &= (8/10)^2 - x^2 - y^2 && \text{quadratic, } \varphi = \varphi_{\text{ex}} \\ \text{case (b): } \varphi &= \text{Proj}_{\mathbb{Q}_2^{C^0}(\mathfrak{K}_h)} \left(8/10 - \sqrt{x^2 - y^2} \right) && \text{signed-distance, } \varphi \neq \varphi_{\text{ex}} \end{aligned}$$

The domain $\Omega = (-3/2, 3/2)^2$ is discretized by 18×18 equidistant quadrilateral cells. Obviously, the exact curvature at the exact interface in this example $\kappa|_{\mathfrak{I}} = -10/8$, and the exact solution to the Poisson problem (8), for $\sigma = 1/10$ is

$$\psi_{\text{ex}} = \begin{cases} 0 & \text{in } \mathfrak{A} \\ 1/8 & \text{in } \mathfrak{B} \end{cases}. \quad (16)$$

Note that in case (a), the quadratic form already is a member of the space $\mathbb{Q}_2^{C^0}(\mathfrak{K}_h)$, therefore the circular interface is represented *exactly* in the polynomial approximation space. In case (b), where this is not the case, the approximation of the circular interface still seems reasonably good: for any \mathbf{x} in the zero-set of φ , the error in the radius, i.e. $|\mathbf{x}|_2 - 8/10$ is less than $1.2 \cdot 10^{-4}$.

However, if in sub-sequence the curvature

$$\kappa := \text{Proj}_{\mathbb{P}_{12}(\mathfrak{K}_h)} (\text{curv}(\nabla\varphi, \partial^2\varphi)) \quad (17)$$

is computed, and the Poisson problem (8) with a right-hand-side based on κ is solved, a quite reasonable error in ψ , and, more severe, $\nabla\psi$ is introduced, which can also be seen in figures 1 and 2:

error type		quadratic	signed-distance
radius	$\forall \mathbf{x} \in \mathfrak{J} : \mathbf{x} _2 - 8/10$	$\leq 10^{-11}$	$\leq 1.2 \cdot 10^{-4}$
curvature	$\forall \mathbf{x} \in \mathfrak{J} : \kappa(\mathbf{x}) - (-10/8)$	$\leq 2.2 \cdot 10^{-9}$	≤ 0.14
pressure	$\ \psi - \psi_{\text{ex}}\ _{L^2(\Omega)}$	$\leq 10^{-10}$	$\approx 1.3 \cdot 10^{-3}$
pressure gradient	$\ \nabla\psi - \nabla\psi_{\text{ex}}\ _{\infty}$	$\leq 2 \cdot 10^{-8}$	≈ 0.4

With respect to the two-phase Navier-Stokes equation, the error in pressure ψ and pressure gradient $\nabla\psi$ are especially inadvertent: from a physical point of view, a circular droplet in a velocity field $\mathbf{u} = 0$ represents a steady state with minimal energy. Since the velocity is linked to the pressure gradient by the momentum equation (1), a non-zero pressure gradient would induce an artificial, non-zero velocity into a state-state solution.

On the other hand, the quadratic test-case basically confirms that the extended DG discretization of the Poisson problem is solved exactly by the numerics, up to machine accuracy. A necessary prerequisite for this is, that that the quadrature rules used to implement the extended DG discretization are sufficiently precise, so that the discretization error is not dominated by the error of the numerical integration.

So, this example demonstrates that the result of a level-set based two-phase computation may heavily depend on the choice of the level-set field. The purpose of this study is to identify filters by which this undesirable dependence can be minimized.

Remark on smooth interface methods: those methods usually treat surface tension as a smoothed Delta-distribution, therefore they do not require $\varphi \in C^0(\Omega)$. However, the discussion on smoothed interface methods is beyond the scope of this publication.

2 Patch recovery in the L^2 – sense.

We introduce the patch-recovery operator

$$\text{prc}_w^l : \mathbb{P}_q(\mathfrak{K}_h) \rightarrow \mathbb{P}_q(\mathfrak{K}_h) \quad (18)$$

which is used to filter the level-set field φ and its derivatives. Some auxiliary definitions are required:

- A cell $K \in \mathfrak{K}_h$ is called to be cut (by the zero-level-set \mathfrak{J}) if $\oint_{K \cap \mathfrak{J}} 1 \, dS \neq 0$.

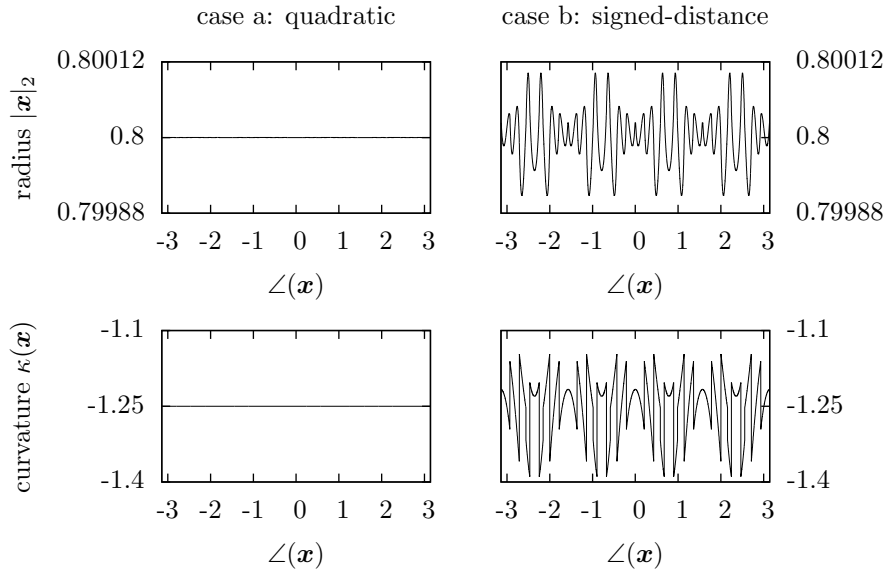


Figure 1: Polar plot of a quadratic versus a signed-distance level-set function φ , for the circular interface with radius 0.8: for points $\mathbf{x} \in \mathcal{J}$, the radius $|\mathbf{x}|_2$ and the curvature at \mathbf{x} , i.e. $\kappa(\mathbf{x})$ are plotted in dependence of the angular coordinate $\angle(\mathbf{x})$. For the quadratic representation, the interface is exact up to round-off errors, yielding a quite accurate representation of the curvature in a piecewise polynomial space with sufficiently high order. On the other hand, for the signed distance representation, an error with a magnitude of about 10^{-4} in the radius yields an L^∞ -error around 10 % in the curvature.

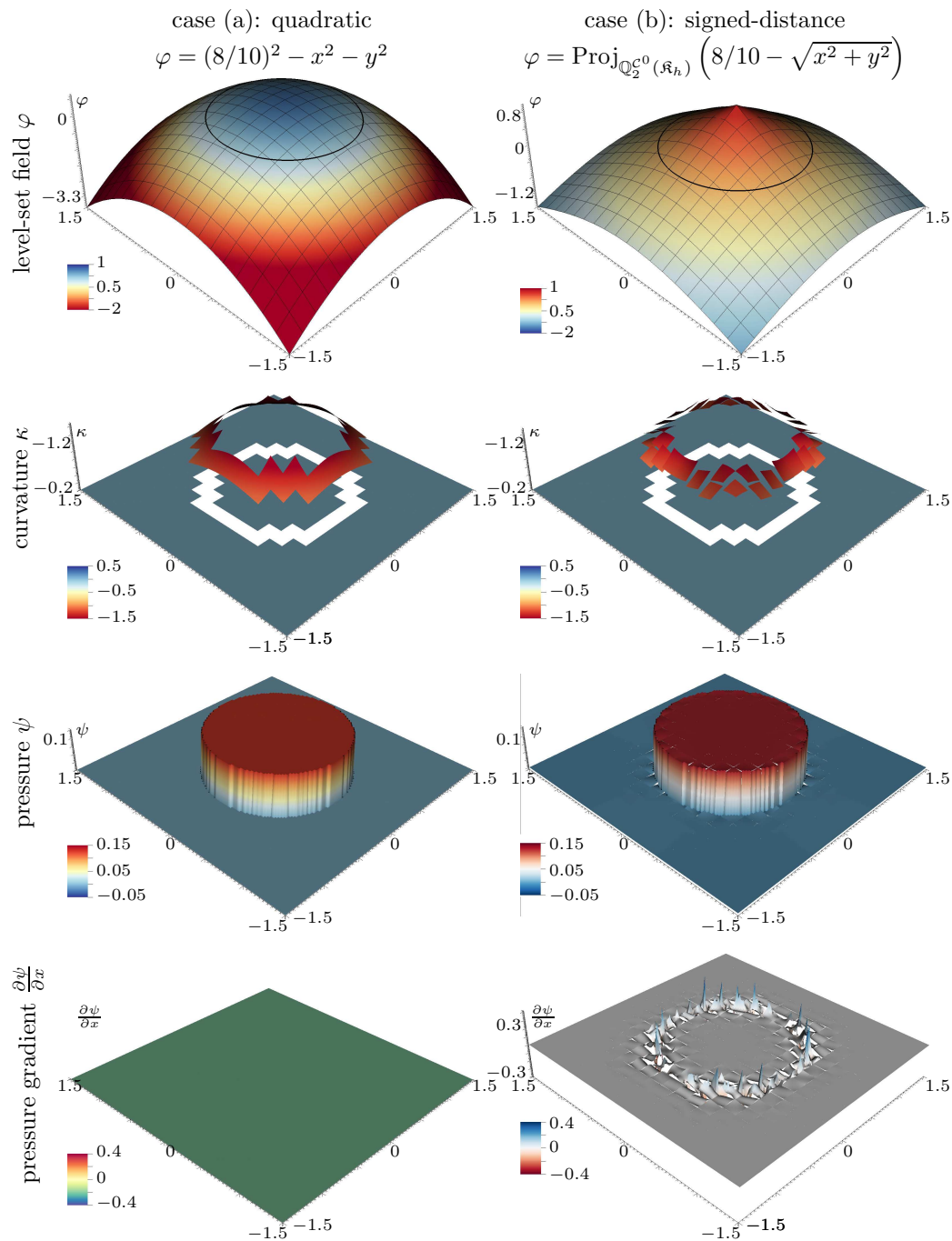


Figure 2: Comparison of a quadratic versus a signed-distance level-set function φ . While the zero level-set of both representation is pretty similar, the error in the curvature κ for case (b) is obvious. In succession, this causes high oscillations in the pressure gradient of the Poisson problem whose right-hand-side depends on κ .

- A cell $L \in \mathfrak{K}_h$ is called to be a neighbor of cell $K \in \mathfrak{K}_h$, if they share at least one point, i.e. if $\overline{L} \cap \overline{K} \neq \{\}$. (Rem.: by defining neighbors as sharing one point – instead of the usual definition of sharing an edge – this e.g. induces that in a Cartesian grid a quadrilateral element has 8 neighbors, and not just 4 as it would be the case with the usual definition of neighbors.)
- We further define the set of all cut-cells,

$$\mathfrak{K}_h^{\text{cc},0} := \{K \in \mathfrak{K}_h; K \text{ is cut}\}$$

and all cut cells and their neighbors

$$\mathfrak{K}_h^{\text{cc},1} := \{K \in \mathfrak{K}_h; K \text{ or one of its neighbors are cut}\}$$

and the union of these cells, i.e.

$$\Omega^{\text{cc},0} := \Omega^{\text{cc}} := \bigcup_{K \in \mathfrak{K}_h^{\text{cc},0}} K \text{ and } \Omega^{\text{cc},1} := \bigcup_{K \in \mathfrak{K}_h^{\text{cc},1}} K.$$

The patch-recovery operator with width $w \in \{0, 1\}$ is defined as the L^2 -projection onto the broken polynomial space on the composite cell Q_K , which is formed from all neighbor cells of some cell K . Precisely: For a cell $K \in \mathfrak{K}_h^{\text{cc},w}$ let be $L_1, \dots, L_I \in \mathfrak{K}_h^{\text{cc},w}$ the neighbors of K in $\mathfrak{K}_h^{\text{cc},w}$. Then one can define a composite cell $Q_K := K \cup L_1 \cup \dots \cup L_I$ and the polynomial space of order q on this composite cell, $\mathbb{P}_q(\{Q_K\})$. For cell K , the patch-recovery operation $\text{prc}_w(u) =: v$ is then defined as the L^2 -projection of u onto $\mathbb{P}_q(\{Q_K\})$, i.e.

$$v|_K := \begin{cases} \text{Proj}_{\mathbb{P}_q(\{Q_K\})}(u|_{Q_K})|_K & \text{if } K \in \mathfrak{K}_h^{\text{cc},w} \\ 0 & \text{if } K \notin \mathfrak{K}_h^{\text{cc},w} \end{cases}.$$

By $\text{prc}_w^l(u)$ we denote the composition of l patch-recovery operations, and consequently $\text{prc}_w^0(u) = u$.

Implementation of the patch-recovery operator: For the space $\mathbb{P}_q(\mathfrak{K}_h)$, we assume an orthonormal basis $(\phi_{j,n})_{j=1,\dots,J,n=1,\dots,N}$, with $\text{supp}(\phi_{j,n}) = \overline{K_j}$. Here j is called the cell-index, while n is called the mode index. Then, one chooses a polynomial basis $(\theta_n)_{n=1,\dots,N}$, on the composite cell Q_K and computes factors A_{nim} to express the basis functions θ_n in terms of ϕ_{jn} , i.e.

$$\theta_n = \sum_{i,m} \phi_{i,m} A_{nim}.$$

l_i denotes a mapping from indices i to the cell indices of the cells which make up Q_K . To aid numerical stability, the basis θ_n may be “pre-orthonormalized”,

e.g. the polynomials may be chosen to be orthonormal in the bounding box of Q_K . For the mass matrix M of θ_n , one gets

$$\begin{aligned} M_{nm} &:= \int_{Q_K} \theta_n \theta_m \, dV \\ &= \sum_{i,s} \sum_{j,r} A_{nis} A_{mjr} \underbrace{\int_{\Omega} \phi_{l_{is}} \phi_{l_{jr}} \, dV}_{=\delta_{ij} \delta_{sr}} \\ &= \sum_{i,r} A_{nir} A_{mir}. \end{aligned}$$

Then, an orthonormal basis on Q_K is given by

$$\vartheta_m = \sum_n \theta_n S_{nm} = \sum_{i,r} \underbrace{\left(\sum_n S_{nm} A_{nir} \right)}_{=: B_{mir}} \phi_{l_{ir}}$$

where the change-of-basis matrix S is given by the relation

$$S^T M S = I, \text{ resp. } M = (S^{-1})^T S^{-1},$$

i.e. S is the inverse of the Cholesky-factor of M . Then, for some function $u = \sum_{j,s} \hat{u}_{l_{js}} \phi_{l_{js}}$, the L^2 -projection of u onto $\mathbb{P}_q(\{Q_K\})$ is given as $v := \sum_n \hat{v}_n \vartheta_n$, with

$$\begin{aligned} \hat{v}_m &= \int_{Q_K} u \vartheta_m \, dV \\ &= \sum_{j,s} \sum_{i,r} \hat{u}_{l_{js}} B_{mir} \underbrace{\int_{Q_K} \phi_{l_{ir}} \phi_{l_{js}} \, dV}_{=\delta_{ij} \delta_{rs}} \\ &= \sum_{j,s} \hat{u}_{l_{js}} B_{mjs}. \end{aligned}$$

Finally, v can be re-expressed in the ‘original’ basis ϕ_{jn} of the space $\mathbb{P}_q(\mathfrak{K}_n)$, within e.g. cell K_{l_1} as

$$v|_{K_{l_1}} = \sum_r \left(\sum_m \hat{v}_m B_{m1r} \right) \phi_{l_{1r}}.$$

The computationally most expensive operation is the construction of the tensors A_{nir} , S_{nm} and finally B_{mir} . Once these are computed, multiple evaluations of the patch-recovery operator are comparatively cheap, since they can be implemented as matrix-vector multiplications.

3 The configurable curvature algorithm and Results

3.1 Test setup

We investigate three basic cases, also shown in figure 3; these are:

$$\begin{aligned}
 \text{case a, large circle:} & \quad \varphi_{\text{ex}} := 0.8 - \sqrt{x^2 + y^2}, \\
 \text{case b, small circle:} & \quad \varphi_{\text{ex}} := 0.25 - \sqrt{x^2 + y^2}, \\
 \text{case c, 'peanut'-shape:} & \quad \varphi_{\text{ex}} := 3 - 0.9 \cos(x) - \sqrt{(x+1)^2 + y^2} \\
 & \quad \quad \quad - \sqrt{(x-1)^2 + y^2}.
 \end{aligned}$$

For case (a) and (b), the domain is chosen as $\Omega = (-3/2, 3/2)$, discretized by 18×18 equidistant cells, while for case (c) $\Omega = (-3, 3) \times (-2, 2)$, discretized by 30×20 equidistant cells. Since we investigate a huge variety of configurations for the curvature algorithm – namely 6144 configurations for each test-case, see below – we do not alter the DG polynomial degree of the level-set function nor of pressure ψ and the pressure gradient. However, the influence of polynomial degree of the curvature approximation κ is investigated, see below. We define the approximation of the exact level-set field φ_{ex} on the broken and the continuous piecewise polynomial space, i.e.

$$\varphi_{\text{br}} := \text{Proj}_{\mathbb{P}_4(\mathfrak{K}_h)}(\varphi_{\text{ex}}) \tag{19}$$

and

$$\varphi_{\mathcal{C}^0} := \text{Proj}_{\mathbb{Q}_2^{\mathcal{C}^0}(\mathfrak{K}_h)}(\varphi_{\text{br}}). \tag{20}$$

For each test case and algorithm configuration, three different L^2 errors are recorded:

$$\begin{aligned}
 \text{curvature on cut-cells:} & \quad \|\kappa - \kappa_{\text{ex}}\|_{L^2(\Omega^{\text{cc}})} \\
 \text{pressure:} & \quad \|\psi - \psi_{\text{ex}}\|_{L^2(\Omega)} \\
 \text{pressure gradient jump:} & \quad \|\llbracket \nabla \psi - \nabla \psi_{\text{ex}} \rrbracket \cdot \mathbf{n}_{\mathcal{T}}\|_{L^2(\mathcal{T})} = \|\llbracket \nabla \psi \rrbracket \cdot \mathbf{n}_{\mathcal{T}}\|_{L^2(\mathcal{T})}
 \end{aligned}$$

The latter error is especially important in the context of a two-phase Navier-Stokes - problem, as already noted in the first example (section 1.4). For a circular interface – which represents, from a physical point of view, a natural minimal-energy state of a droplet – one usually wants the pressure gradient $\nabla \psi$ as low as possible. A non-zero pressure gradient would correspond to some ‘artificial’ velocity that is introduced in the momentum equation (1), preventing the simulation from reaching the natural, minimal-energy final state with zero velocity.

Evaluation of curvature: When applying patch-recovery construction to curvature-evaluation, several options are at hand: Where in the algorithm should patch-recovery be applied? Onto the input, i.e. the level-set function, onto the output, i.e. the curvature, onto intermediate results like gradients or

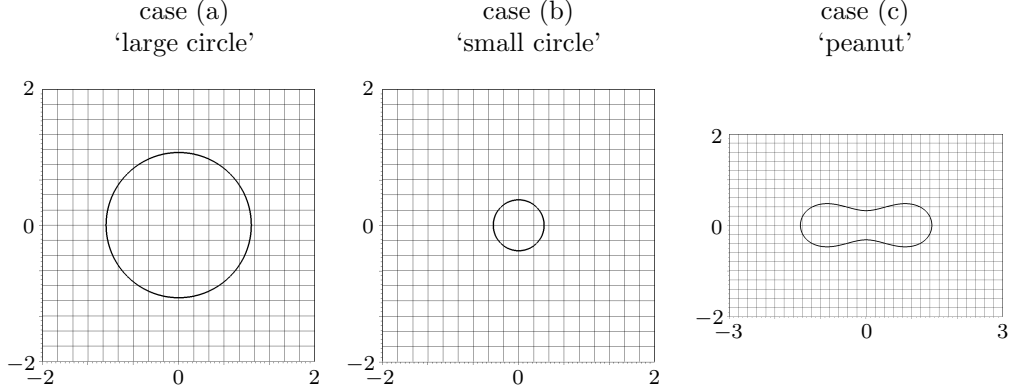


Figure 3: The three different test geometries which are investigated: a rather large circle, with respect to grid width h , a small circle and a 'peanut'-shaped interface.

Hessians, or everywhere? Which polynomial degree should be chosen for the curvature? How many cells around the interface should be used for the patch recovery operation?

In order to evaluate different configurations for patch recovery – based curvature algorithms, a modular algorithm with the following options was implemented; the filtered curvature $\tilde{\kappa}$, used as an input to the Poisson problem (8), resp. (22), is computed as

$$\begin{cases}
 f := \text{one of } \begin{cases} \varphi_{C^0} \\ \varphi_{br} \end{cases} \\
 \tilde{f} := \text{prc}_w^{l_1}(f) \\
 \mathbf{g} := \text{one of } \begin{cases} \nabla f \\ \nabla \tilde{f} \end{cases} \\
 \tilde{\mathbf{g}} := \text{prc}_w^{l_1}(\mathbf{g}) \\
 \mathbf{H} := \text{one of } \begin{cases} \partial^2 f \\ \nabla \mathbf{g} \\ \partial^2 \tilde{f} \\ \nabla \tilde{\mathbf{g}} \end{cases} \\
 \tilde{\mathbf{H}} := \text{prc}_w^{l_1}(\mathbf{H}) \\
 \kappa := \text{curv} \left(\text{one of } \begin{cases} \mathbf{g} \\ \tilde{\mathbf{g}} \end{cases}, \text{one of } \begin{cases} \mathbf{H} \\ \tilde{\mathbf{H}} \end{cases} \right) \\
 \tilde{\kappa} := \text{prc}_w^{l_2}(\kappa)
 \end{cases} \quad (21)$$

A flowchart is given in figure 4. In detail, this algorithm provides the following configuration options:

- Which field should be used as an input for the algorithm (switch ' $f = ?$ ')?
 - the SEM-representation (case ' φ_{C^0} '), i.e. $f := \varphi_{C^0}$.

- the DG-representation (case ‘ φ_{br} ’), i.e. $f := \varphi_{\text{br}}$.
- From which field should the level-set gradient \mathbf{g} be computed (switch ‘ $\mathbf{g}=?$ ’)?
 - from the un-filtered level-set (case ‘ ∇f ’), i.e. $\mathbf{g} := \nabla f$.
 - from the filtered level-set (case ‘ $\nabla \tilde{f}$ ’), i.e. $\mathbf{g} := \nabla \tilde{f}$.
- From which field should the Hessian \mathbf{H} of the level-set be computed (switch ‘ $\mathbf{H}=?$ ’)?
 - from the un-filtered level-set (case ‘ $\partial^2 f$ ’), i.e. $\mathbf{H} := \partial^2 f$.
 - from the un-filtered level-set gradient (case ‘ $\nabla \mathbf{g}$ ’), i.e. $\mathbf{H} := \nabla \mathbf{g}$.
 - from the filtered level-set (case ‘ $\partial^2 \tilde{f}$ ’), i.e. $\mathbf{H} := \partial^2 \tilde{f}$.
 - from the filtered level-set gradient (case ‘ $\nabla \tilde{\mathbf{g}}$ ’), i.e. $\mathbf{H} := \nabla \tilde{\mathbf{g}}$.
- The number $l_1 \in \{1, 2, 5, 10\}$ of patch-recovery-cycles that are applied to the level-set field and its derivatives, i.e. $\tilde{f} := \text{prc}^{l_1}(f)$, $\tilde{\mathbf{g}} := \text{prc}^{l_1}(\mathbf{g})$ and $\tilde{\mathbf{H}} := \text{prc}^{l_1}(\mathbf{H})$.
- The number $l_2 \in \{0, 1, 5, 10\}$ of patch-recovery-cycles that are applied to the computed curvature κ i.e. $\tilde{\kappa} := \text{prc}^{l_2}(\kappa)$.
- The DG-polynomial degree of the curvature κ and the filtered derivatives is altered: $\kappa, \tilde{\kappa}, \tilde{f} \in \mathbb{P}_{\alpha p}(\mathfrak{K}_h)$, $\tilde{\mathbf{g}} \in \mathbb{P}_{\alpha p}(\mathfrak{K}_h)^2$, $\tilde{\mathbf{H}} \in \mathbb{P}_{\alpha p}(\mathfrak{K}_h)^{2 \times 2}$, where $p = 4$ is the polynomial degree of φ_{DG} , with the integer multiplier $\alpha \in \{1, 2, 3\}$.

3.2 Results and discussion

For all test-cases, the three different errors measures span across several magnitudes, see figures 5 and 6, with one exception, namely the error $\|\psi - \psi_{\text{ex}}\|_{L^2(\Omega)}$ in case (c), see bottom-left plot in figure 6. Therefore, the pressure error of case (c) is not considered in the survey.

- It is, in all test-cases generally better to use the DG-representation ($f = \varphi_{\text{br}}$) for curvature computation than the continuous CG ($f = \varphi_{\text{C}^0}$). Considering that the broken approximation $\varphi_{\text{br}} \in \mathbb{P}_4(\mathfrak{K}_h)$ is in general more precise than the continuous approximation $\varphi_{\text{C}^0} \in \mathbb{Q}_2^{\text{C}^0}(\mathfrak{K}_h)$, this seems not very surprising:

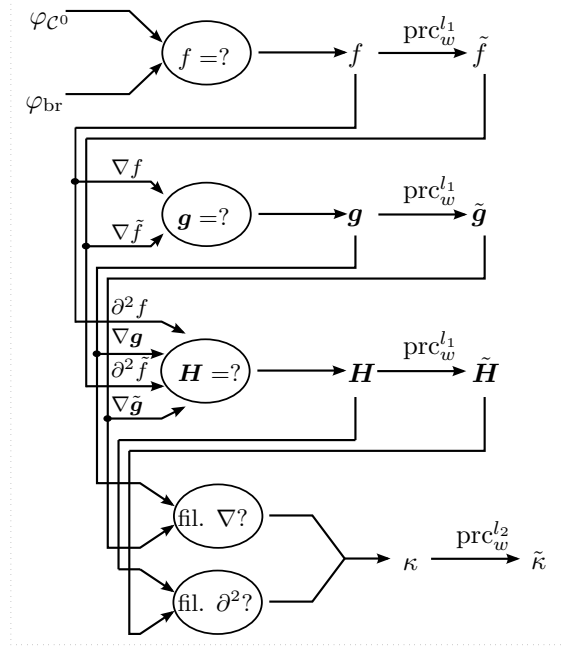


Figure 4: Flow chart for curvature evaluation: the filtered curvature $\tilde{\kappa}$ is computed either from the SEM (φ_{C^0}) or the DG (φ_{br}) representation of the level-set field. The configuration of the algorithm depends on the switches for the level-set source ($f=?$), for the gradient source ($g=?$), for the Hessian source ($H=?$), on the number of patch-recovery cycles for the derivatives (l_1) and the curvature itself (l_2), as well as the width w of the patch-recovery domain; furthermore, there are switches (fil. $\nabla?$, fil. $\partial^2?$) to evaluate Bonnet's formula from either the un-filtered gradient g or the filtered gradient \tilde{g} and, independently from either the un-filtered Hessian H or the filtered Hessian \tilde{H} . In addition, not shown in this graph, we vary the DG polynomial degree of \tilde{f} , \tilde{g} , \tilde{H} , κ and $\tilde{\kappa}$ as well as the domain of the patch-recovery.

	$\ \varphi_{\text{br}} - \varphi_{\text{ex}}\ _{L^2(\Omega^{\text{cc}})}$	$\ \varphi_{\mathcal{C}^0} - \varphi_{\text{ex}}\ _{L^2(\Omega^{\text{cc}})}$
case (a)	$3.192 \cdot 10^{-7}$	$5.087 \cdot 10^{-5}$
case (b)	$1.165 \cdot 10^{-5}$	$2.396 \cdot 10^{-4}$
case (c)	$1.71 \cdot 10^{-5}$	$3.759 \cdot 10^{-4}$
	$\ \nabla\varphi_{\text{br}} - \nabla\varphi_{\text{ex}}\ _{(L^2(\Omega^{\text{cc}}))^2}$	$\ \nabla\varphi_{\mathcal{C}^0} - \nabla\varphi_{\text{ex}}\ _{(L^2(\Omega^{\text{cc}}))^2}$
case (a)	$3.128 \cdot 10^{-5}$	$2.008 \cdot 10^{-3}$
case (b)	$1.096 \cdot 10^{-3}$	$1.096 \cdot 10^{-2}$
case (c)	$1.342 \cdot 10^{-3}$	$1.418 \cdot 10^{-2}$
	$\ \partial^2\varphi_{\text{br}} - \partial^2\varphi_{\text{ex}}\ _{(L^2(\Omega^{\text{cc}}))^{2 \times 2}}$	$\ \partial^2\varphi_{\mathcal{C}^0} - \partial^2\varphi_{\text{ex}}\ _{(L^2(\Omega^{\text{cc}}))^{2 \times 2}}$
case (a)	$2.173 \cdot 10^{-3}$	$9.045 \cdot 10^{-2}$
case (b)	$7.806 \cdot 10^{-2}$	$4.364 \cdot 10^{-1}$
case (c)	$7.958 \cdot 10^{-2}$	$4.71 \cdot 10^{-1}$

The minimal errors achieved for the broken and the continuous approximation, over all configurations are:

	min. over configs. with broken approx. ($f = \varphi_{\text{br}}$)	min. over configs. with continuous approx. ($f = \varphi_{\mathcal{C}^0}$)
curvature error $\ \kappa - \kappa_{\text{ex}}\ _{L^2(\Omega^{\text{cc}})}$:		
case (a)	$1.874 \cdot 10^{-5}$	$8.008 \cdot 10^{-4}$
case (b)	$3.821 \cdot 10^{-3}$	$3.606 \cdot 10^{-2}$
case (c)	$5.46 \cdot 10^{-3}$	$6.43 \cdot 10^{-2}$
pressure error $\ \psi - \psi_{\text{ex}}\ _{L^2(\Omega)}$:		
case (a)	$1.053 \cdot 10^{-6}$	$1.697 \cdot 10^{-5}$
case (b)	$2.669 \cdot 10^{-5}$	$6.34 \cdot 10^{-5}$
case (c)	$1.403 \cdot 10^{-1}$	$1.542 \cdot 10^{-1}$
pressure gradient jump error $\ \llbracket \nabla\psi \rrbracket \cdot \mathbf{n}_{\mathcal{J}}\ _{L^2(\mathcal{J})}$:		
case (a)	$1.928 \cdot 10^{-4}$	$4.19 \cdot 10^{-4}$
case (b)	$2.519 \cdot 10^{-3}$	$3.916 \cdot 10^{-3}$
case (c)	$5.966 \cdot 10^{-2}$	$5.454 \cdot 10^{-2}$

Most interestingly, the latter error measure, $\|\llbracket \nabla\psi \rrbracket \cdot \mathbf{n}_{\mathcal{J}}\|_{L^2(\mathcal{J})}$, seems not to be affected by the choice of broken versus continuous approximation.

- Regarding performance, the most influential factors are – not surprisingly – the polynomial order of the curvature approximation space $\mathbb{P}_{4\alpha}(\mathfrak{K}_h)$, and the width w of the patch-recovery domain. The major computational cost of the patch-recovery operator is the construction of the projector onto the aggregate cells, while the evaluation of the patch-recovery is in comparison quite fast. Therefore, the number of patch-recovery cycles l_1 and l_2 is only of minor influence to the run-time. For all algorithm configurations which employ any kind of patch-recovery, we observe the

following mean run-times $\mu_{t_{\text{run}},\alpha,w}$ and standard deviations $\sigma_{t_{\text{run}},\alpha,w}$, for different (α, w) - pairs:

$(\alpha, w) \rightarrow$		1,0	1,1	2,0	2,1	3,0	3,1	
case (a)	$\mu_{t_{\text{run}},\alpha,w}$	0.29	0.7	1.3	6.2	9.0	48	seconds
	$\sigma_{t_{\text{run}},\alpha,w}$	0.53	0.84	1.1	2.5	3.0	6.9	seconds
	$\left(\frac{\mu_{t_{\text{run}},\alpha,w}}{\mu_{t_{\text{run}},1,0}}\right)$	1.0	2.5	4.5	22	32	168	normalized
	$\left(\frac{\sigma_{t_{\text{run}},\alpha,w}}{\mu_{t_{\text{run}},1,0}}\right)$	1.9	2.9	4.0	8.7	10	24	normalized
case (b)	$\mu_{t_{\text{run}},\alpha,w}$	0.24	0.38	0.62	2.4	3.9	17	seconds
	$\sigma_{t_{\text{run}},\alpha,w}$	0.49	0.62	0.79	1.5	2.0	4.1	seconds
	$\left(\frac{\mu_{t_{\text{run}},\alpha,w}}{\mu_{t_{\text{run}},1,0}}\right)$	1.0	1.6	2.6	9.7	16	71	normalized
	$\left(\frac{\sigma_{t_{\text{run}},\alpha,w}}{\mu_{t_{\text{run}},1,0}}\right)$	2.0	2.5	3.2	6.3	8.1	17	normalized
case (c)	$\mu_{t_{\text{run}},\alpha,w}$	0.25	0.62	1.3	7.6	11	63	seconds
	$\sigma_{t_{\text{run}},\alpha,w}$	0.50	0.79	1.2	2.7	3.4	8.0	seconds
	$\left(\frac{\mu_{t_{\text{run}},\alpha,w}}{\mu_{t_{\text{run}},1,0}}\right)$	1.0	2.5	5.4	31	46	257	normalized
	$\left(\frac{\sigma_{t_{\text{run}},\alpha,w}}{\mu_{t_{\text{run}},1,0}}\right)$	2.0	3.2	4.7	11	14	32	normalized

It becomes apparent that especially the cases with $(\alpha, w) = (3, 0)$ and $(\alpha, w) = (3, 1)$ are computationally expensive: among all test-cases, the $(\alpha, w) = (3, 0)$ - configurations are between 16 and 38 times more expensive than the $(\alpha, w) = (1, 0)$ - configuration; for the $(\alpha, w) = (3, 1)$ - configurations that factor is 71 and 257.

- For all test-cases, no significant improvement in the errors $\|\psi - \psi_{\text{ex}}\|_{L^2(\Omega)}$ and $\|(\nabla\psi - \nabla\psi_{\text{ex}}) \cdot \mathbf{n}_{\mathcal{J}}\|_{L^2(\mathcal{J})}$ could be observed for $\alpha > 2$ and $w > 0$. Furthermore, no significant improvement could be obtained by any kind of filtering of Level-Set gradient or Hessian, nor by filtering the curvature itself. Indeed, from figures 5 and 6, it becomes obvious that configurations (marked as • in cited figures) which

- use the broken polynomial-level-set field ($f = \varphi_{\text{br}}$),
- perform patch recover only on cut cells itself ($w = 0$),
- use polynomial degree $2 \cdot p$ for \tilde{f} and κ ($\alpha = 2$),
- compute gradient and Hessian from the filtered level-set field ($\mathbf{g} = \nabla\tilde{f}$, $\mathbf{H} = \partial^2\tilde{f}$),
- employ no additional filtering of the gradient nor the Hessian (fil. $\nabla = \text{false}$, fil. $\partial^2 = \text{false}$) and
- employ no additional filtering of computed curvature ($l_2 = 0$)

are among the best-performing and fastest configurations for test cases, with respect to each error measure.

- As obvious from figures 5 and 6, there are certain configurations which perform better in certain test cases. However, there are no configurations which perform significantly better overall, i.e. with respect to all three error measures in all three test cases. In order to check that, we selected the 10 fastest configurations out of the 100 best-performing, with respect to the three different error measures in all test-cases. From those configurations, which performed well overall, none significantly out-performed the configuration recommendation given above.
- Finally, we perform a separate discussion of those configurations which use the continuous representation of the level-set field ($f = \varphi_{C^0}$). While φ_{C^0} itself is continuous, its first and second derivatives contain higher levels of oscillations than the broken polynomial representation φ_{br} of the level-set field, as already noted above. Here, filtering of the gradient \mathbf{g} and the Hessian \mathbf{H} provide a significant improvement. The top-5 configurations overall are:

$\mathbf{g} = ?$	$\mathbf{H} = ?$	fil. $\nabla?$	fil. $\partial^2?$	α	w	l_1	l_2
$\nabla \tilde{f}$	$\nabla \tilde{\mathbf{g}}$	true	true	1	0	1	0
$\nabla \tilde{f}$	$\nabla \tilde{\mathbf{g}}$	true	true	1	0	1	1
$\nabla \tilde{f}$	$\nabla \tilde{\mathbf{g}}$	true	false	1	0	1	1
$\nabla \tilde{f}$	$\nabla \tilde{\mathbf{g}}$	false	false	1	0	1	1
$\nabla \tilde{f}$	$\nabla \tilde{\mathbf{g}}$	false	false	1	0	2	1

Common for all of these cases is that the gradient \mathbf{g} is computed from the filtered level \tilde{f} , the Hessian \mathbf{H} is computed from the filtered gradient $\tilde{\mathbf{g}}$, the best results were quite surprisingly achieved for lower order approximation spaces (i.e. $\alpha = 1$, i.e. $\tilde{f}, \tilde{\mathbf{g}}, \tilde{\mathbf{H}}, \kappa, \tilde{\kappa}$ are of DG-polynomial order $1 \cdot \alpha$) and that the width of the patch-recovery domain $w = 0$. The performance of these top-5 configuration is visualized in the scatter plots figure 7 and 8.

4 Conclusions and outlook.

A very important result of this survey is first, that we found that there is no need to increase the polynomial degree of the filtered properties by more than a factor of two times, in comparison to the polynomial degree of the original level-set field; second, that we found it sufficient to perform the patch recovery just on the layer of cut-cells themselves, and not considering any values outside of that band. Since the run-time is dominated by those two factors, it is very pleasant that these factors can be kept low.

Furthermore, we were able to show the additional benefit of filtering also the gradient and the Hessian in the case of the spectral-element representation of the level set.

Within this study we focused on the curvature computation in a very controlled setup, where an analytic expression for the level-set field was given.

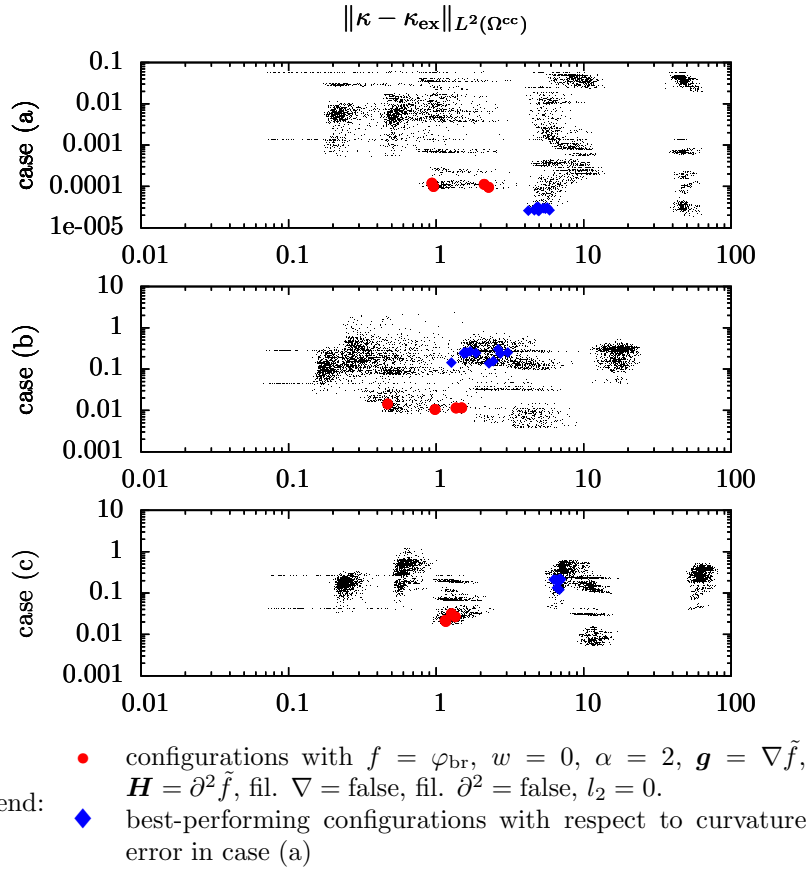


Figure 5: A scatter plot, showing all algorithm configurations, for all test cases, presenting the run-time of the curvature evaluation versus the error measure $\|\kappa - \kappa_{\text{ex}}\|_{L^2(\Omega^{\text{cc}})}$. Configurations marked with symbol \bullet are overall well-performing, i.e. they are among the most accurate and fastest configurations for each of the three error measures and all test cases, see also figure 6. There are certainly configurations, like the ones marked by \blacklozenge , which perform better in a specific test-case, but not overall.

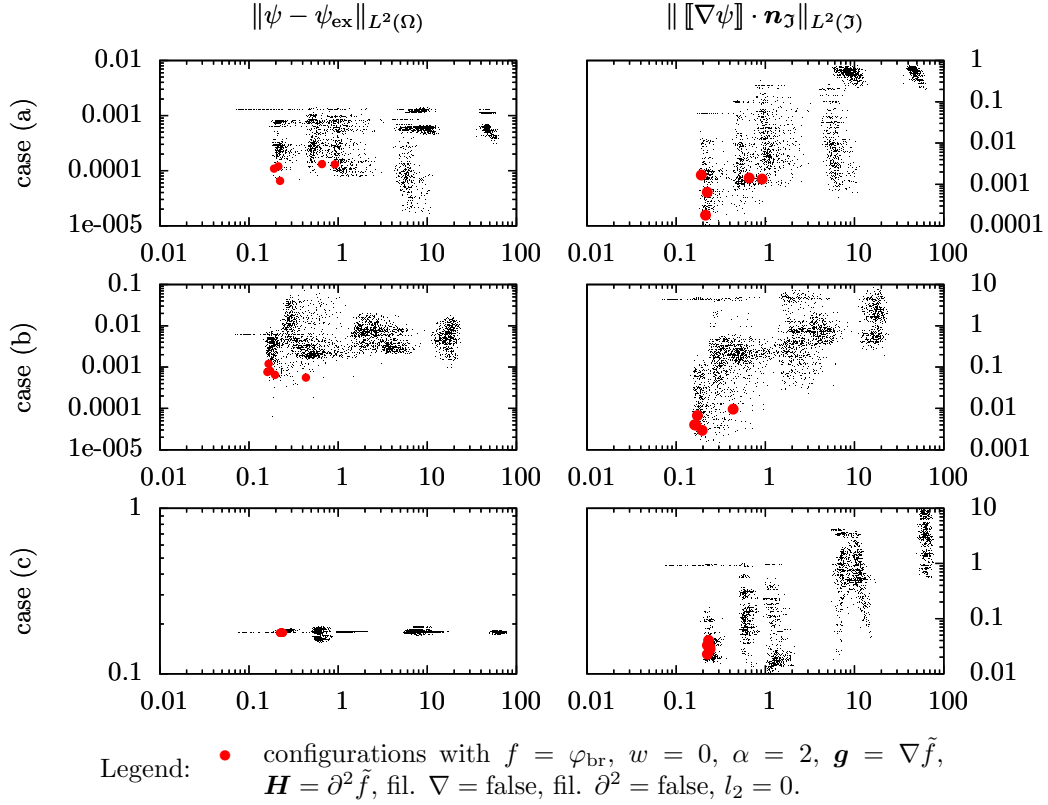
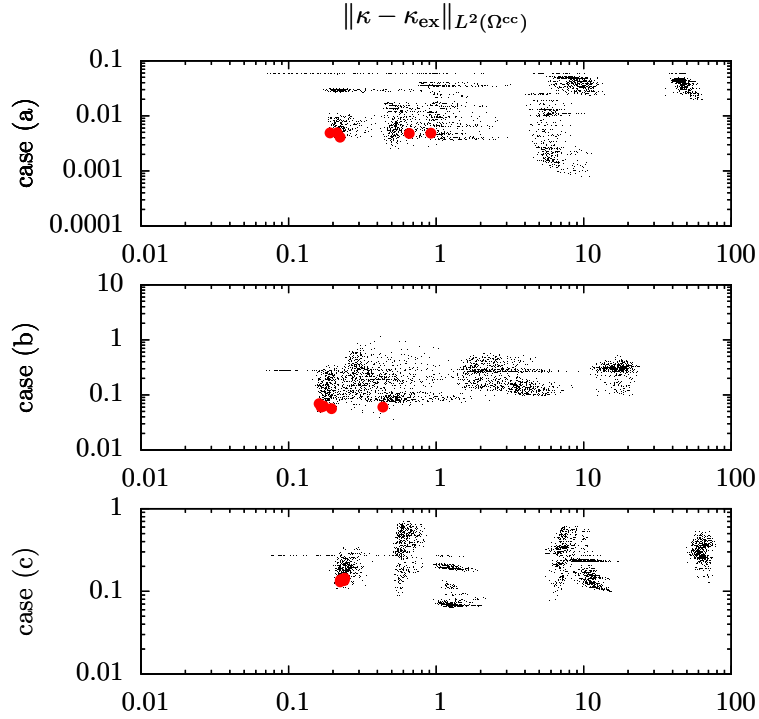


Figure 6: A scatter plot, showing all algorithm configurations, for all test cases, presenting the run-time of the curvature evaluation versus the two different error measures $\|\psi - \psi_{\text{ex}}\|_{L^2(\Omega)}$ and $\| \llbracket \nabla \psi \rrbracket \cdot \mathbf{n}_J \|_{L^2(\mathcal{J})}$. Configurations marked with symbol • are overall well-performing, i.e. they are among the most accurate and fastest configurations for each of the three error measures and all test cases, see also figure 5.



Legend: • top-5 configurations overall; common configuration settings are: $\mathbf{g} = \nabla f$, $\mathbf{H} = \nabla \hat{\mathbf{g}}$, $\alpha = 1$, $w = 0$.

Figure 7: A scatter plot, showing all algorithm configurations which use the continuous representation of the level-set ($f = \varphi_{C^0}$), for all test cases, presenting the run-time of the curvature evaluation versus the error measure $\|\kappa - \kappa_{\text{ex}}\|_{L^2(\Omega^{\text{cc}})}$. Configurations marked with symbol \bullet are overall well-performing, i.e. they are among the most accurate and fastest configurations for each of the three error measures and all test cases, see also figure 8. There are certainly configurations, like the ones marked by \times , which perform better in a specific test-case, but not overall.

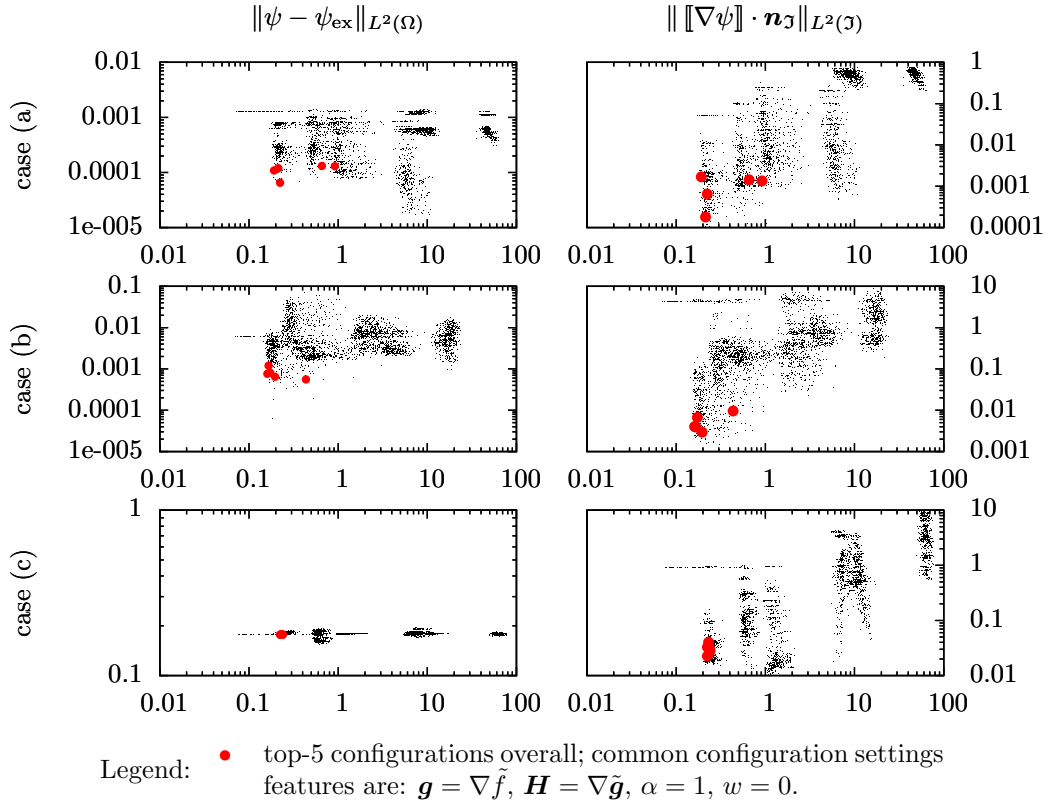


Figure 8: A scatter plot, showing all algorithm configurations which use the continuous representation of the level-set ($f = \varphi_{\mathcal{C}^0}$), for all test cases, presenting the run-time of the curvature evaluation versus the two different error measures $\|\psi - \psi_{\text{ex}}\|_{L^2(\mathcal{J})}$ and $\|[\![\nabla p]\!] \|_{L^2(\mathcal{J})}$. Configurations marked with symbol \bullet are overall well-performing, i.e. they are among the most accurate and fastest configurations for each of the three error measures and all test cases, see also figure 7.

We are currently developing a two-phase Navier-Stokes solver based on the extended DG discretization presented in section A where curvature computation is an important part.

This survey focused solely on patch recovery for filtering DG-based properties. Obviously, there other techniques for constructing filters, e.g. WENO, which we may investigate in future works.

A Extended DG discretization of the Poisson problem

Finally, we give a brief description of the extended discontinuous Galerkin method which is used to solve the Poisson eq. (8). We search for $(\psi, \mathbf{v}) \in \mathbb{P}_2^X(\mathfrak{K}_h) \times \mathbb{P}_3^X(\mathfrak{K}_h)^2$, so that for all $(f, \mathbf{w}) \in \mathbb{P}_2^X(\mathfrak{K}_h) \times \mathbb{P}_3^X(\mathfrak{K}_h)^2$

$$\begin{aligned} b(\psi, \mathbf{w}) &= s(\mathbf{w}) \\ b(f, \mathbf{w}) &= 0 \end{aligned} \tag{22}$$

The bilinear form $b(-, -)$ is given as

$$b(f, \mathbf{w}) = - \int_{\Omega} f \operatorname{div}(\mathbf{w}) \, d\mathbf{x} - \oint_{\Gamma \cup \mathfrak{I}} \llbracket \mathbf{v} \rrbracket \cdot \mathbf{n}_{\mathfrak{I}, \Gamma} \{ \{ p \} \} \, dS.$$

while the linear form $s(-)$, which represents the surface-tension terms, is given as

$$s(\mathbf{w}) = \oint_{\mathfrak{I}} \sigma \tilde{\kappa} \mathbf{n}_{\mathfrak{I}} \cdot \llbracket \mathbf{w} \rrbracket \, dS.$$

Again, ∇ denotes also the broken gradient, and $\operatorname{div}(-)$ the broken divergence. The set Γ is the union of all edges of all cells, i.e. $\Gamma := \bigcup_{K \in \mathfrak{K}_h} \partial K$ and $\mathbf{n}_{\mathfrak{I}, \Gamma}$ denotes an almost-everywhere continuous normal field, which is equal to $\mathbf{n}_{\mathfrak{I}}$ on \mathfrak{I} , an outer normal on $\partial\Omega$ and normal onto the cell boundaries. Given that, the jump- and mean-value operator are defined as

$$\begin{aligned} \llbracket u \rrbracket(\mathbf{x}) &:= \lim_{\xi \searrow 0} (u(\mathbf{x} + \xi \mathbf{n}_{\mathfrak{I}, \Gamma}) - u(\mathbf{x} - \xi \mathbf{n}_{\mathfrak{I}, \Gamma})) && \text{on } (\Gamma \setminus \partial\Omega) \cup \mathfrak{I}, \\ \{ \{ u \} \}(\mathbf{x}) &:= \lim_{\xi \searrow 0} \frac{1}{2} (u(\mathbf{x} + \xi \mathbf{n}_{\Gamma}) + u(\mathbf{x} - \xi \mathbf{n}_{\Gamma})) && \text{on } (\Gamma \setminus \partial\Omega) \cup \mathfrak{I}, \\ \llbracket u \rrbracket(\mathbf{x}) &:= \lim_{\xi \searrow 0} u(\mathbf{x} - \xi \mathbf{n}_{\mathfrak{I}, \Gamma}) && \text{on } \partial\Omega, \\ \{ \{ u \} \}(\mathbf{x}) &:= \lim_{\xi \searrow 0} u(\mathbf{x} - \xi \mathbf{n}_{\mathfrak{I}, \Gamma}) && \text{on } \partial\Omega. \end{aligned}$$

In order to perform numerical integration on the cut cells, i.e. on domains like $K \cap \mathfrak{A}$, $K \cap \mathfrak{B}$, $K \cap \mathfrak{I}$, etc., a quadrature technique presented in [11] is used. The linear system obtained from discretization (22) is solved by the direct sparse solver PARDISO, see [15, 13, 14].

References

- [1] T. Chen, P. D. Mineev, and K. Nandakumar. A projection scheme for incompressible multiphase flow using adaptive eulerian grid. *International*

Journal for Numerical Methods in Fluids, 45:1–19, May 2004. ISSN 0271-2091, 1097-0363.

- [2] K.-W. Cheng and T.-P. Fries. XFEM with hanging nodes for two-phase incompressible flow. *Computer Methods in Applied Mechanics and Engineering*, 245-246:290–312, 2012. ISSN 00457825. doi: 10.1016/j.cma.2012.07.011. URL <http://linkinghub.elsevier.com/retrieve/pii/S0045782512002319>.
- [3] D. A. Di Pietro and A. Ern. *Mathematical Aspects of Discontinuous Galerkin Methods*. Number 69 in Mathématiques et Applications. Springer, 2011. ISBN 9783642229794.
- [4] S. Gross and A. Reusken. Finite element discretization error analysis of a surface tension force in two-phase incompressible flows. *SIAM J. Numer. Anal.*, 45(4):1679–1700, 2007.
- [5] F. Heimann. *An Unfitted Higher-Order Discontinuous Galerkin Method for Incompressible Two-Phase Flow with Moving Contact Lines*. PhD thesis, Heidelberg University, Heidelberg, 2013.
- [6] F. Heimann, C. Engwer, O. Ippisch, and P. Bastian. An unfitted interior penalty discontinuous Galerkin method for incompressible Navier-Stokes two-phase flow. *International Journal for Numerical Methods in Fluids*, 71(3):269–293, 2013. ISSN 02712091. doi: 10.1002/flid.3653. URL <http://doi.wiley.com/10.1002/flid.3653>.
- [7] M. Herrmann. On simulating primary atomization using the refined level set grid method. *Atomization and Sprays*, 21(4):283–301, 2011. ISSN 1044-5110. doi: 10.1615/AtomizSpr.2011002760. URL <http://www.begellhouse.com/journals/6a7c7e10642258cc,4fa736af31a9c3d7,32765dc85aa6de1e>.
- [8] M. Herrmann and Z. Jibben. A Runge-Kutta discontinuous Galerkin conservative level set method. In *Center for Turbulence Research, Annual Research Briefs 2012*, pages 305–314, 2012. URL http://ctr.stanford.edu/Summer/SP12/05.01_jibben.pdf.
- [9] J. S. Hesthaven and T. Warburton. *Nodal Discontinuous Galerkin Methods: Algorithms, Analysis, and Applications*. Number 54 in Texts in Applied Mathematics. Springer-Verlag, 2008. ISBN 978-0-387-72065-4.
- [10] K. Hutter and K. D. Jöhnk. *Continuum methods of physical modeling: continuum mechanics, dimensional analysis, turbulence*. Springer, Berlin, 2004. ISBN 3540206191 9783540206194.
- [11] B. Müller, F. Kummer, and M. Oberlack. Highly accurate surface and volume integration on implicit domains by means of moment-fitting. *Int. J. Numer. Meth. Eng.*, pages 512–528, 2013. ISSN 00295981. doi: 10.1002/nme.4569.

- [12] H. Sauerland and T.-P. Fries. The stable XFEM for two-phase flows. *Computers & Fluids*, 87:41–49, 2013. ISSN 00457930. doi: 10.1016/j.compfluid.2012.10.017. URL <http://linkinghub.elsevier.com/retrieve/pii/S0045793012004148>.
- [13] O. Schenk. Solving unsymmetric sparse systems of linear equations with PARDISO. *Future Generation Computer Systems*, 20(3):475–487, 2004. ISSN 0167739X. doi: 10.1016/j.future.2003.07.011.
- [14] O. Schenk and K. Gärtner. On fast factorization pivoting methods for sparse symmetric indefinite systems. *Electronic Transactions on Numerical Analysis*, 23:158–179, 2006.
- [15] O. Schenk, K. Gärtner, and W. Fichtner. Efficient sparse LU factorization with Left-Right looking strategy on shared memory multiprocessors. *BIT Numerical Mathematics*, 40(1):158–176, 2000. ISSN 0006-3835.
- [16] Y. Wang and M. Oberlack. A thermodynamic model of multiphase flows with moving interfaces and contact line. *Continuum Mechanics and Thermodynamics*, 23:409–433, May 2011. ISSN 0935-1175, 1432-0959.
- [17] O. Zienkiewicz and J. Zhu. The superconvergent patch recovery (SPR) and adaptive finite element refinement. *Computer Methods in Applied Mechanics and Engineering*, 101(1-3):207–224, 1992. ISSN 00457825. doi: 10.1016/0045-7825(92)90023-D. URL <http://linkinghub.elsevier.com/retrieve/pii/004578259290023D>.